International Journal of Basic and Applied Sciences, 14 (1) (2025) 350-363

International Journal of Basic and Applied Sciences

Website: www.sciencepubco.com/index.php/IJBAS
https://doi.org/10.14419/q8mswr85
Research paper

High-efficiency EV charging system using Zeta-Cuk converter with optimized MPPT and power management

J. Viswanatha Rao [1] *, D. Karthikeyan [2], Sujatha Balaraman [3], J. Raji [4]

[1] Professor, Department of Electrical and Electronics Engineering, VNR Vignana Jyothi Institute of Engineering & Technology, Hyderabad, India.
[2] Assistant Professor, Department of Electrical and Electronics Engineering, SRM institute of science and technology, Kattankulathur 603203, Chennai, India.
[3] Professor, Department of Electrical and Electronics Engineering, Government College of Engineering, Bodinayakanur-625582, India.
[4] Assistant Professor, Department of Electrical and Electronics Engineering, Bharath Institute of Higher Education and Research, Chennai 600073, India.
**Corresponding author E-mail: viswanath72@gmail.com*

Received: March 25, 2025, Accepted: April 30, 2025, Published: May 24 2025

Abstract

Due to the growing demand for efficient and sustainable energy solutions for Electric Vehicles (EVs) powered by Brushless DC (BLDC) motors, this work presents a high-efficiency EV charging system that integrates renewable energy through a high-gain Zeta-Cuk converter and advanced power management. The converter boosts the low voltage from photovoltaic (PV) panels to a high DC bus level, ensuring efficient energy transfer. To maximize power extraction an optimized Maximum Power Point Tracking (MPPT) method, combining the Ant Lion Optimization (ALO) algorithm with an Adaptive Neuro-Fuzzy Inference System (ANFIS), is used. A storage battery and grid connection are incorporated to manage surplus energy during periods of excess PV generation. Power flow between the grid, battery and BLDC motor is coordinated via a bidirectional DC-DC converter controlled by a Proportional-Integral (PI) controller. The system is validated through MATLAB/Simulink simulations, demonstrating a high conversion efficiency of 96.69% and a tracking efficiency of 99.21%, confirming its potential as a practical and eco-friendly solution for sustainable transportation.

Keywords: *Electric Vehicles; BLDC Motor; Photovoltaic; High-Gain Zeta-Cuk Converter; MPPT; ALA-ANFIS; Bidirectional DC-DC Converter; PI Controller.*

1. Introduction

Since EVs are becoming more and more popular as a sustainable mode of transportation, it is critical to establish dependable and effective charging infrastructure. An electric vehicle's motor is one of its essential propulsion components, and the BLDC has become the industry standard because of its exceptional torque characteristics and great efficiency [1-2]. Demands for RES are essential for BLDC motor owing to the ongoing depletion of fossil fuels [3]. PV systems are well-suited for BLDC motors [4]. PV systems have also been remarkably used to generate electricity for EV [5]. However, the main issues of PV systems are variations in solar insolation level [6].
MPPT techniques are a crucial component for rapid and precise tracking and the capability to produce peak power [7]. Various classical approaches such as Incremental Conductance (INC) [8], Hill Climbing (HC) [9], and Perturb and Observe (P&O) [10]. However, when the weather is not consistent, the algorithms lose control [11]. Intelligent MPPT algorithms have been used to extract peak power in sudden operating situations, including Artificial Neural Network (ANN) [12], RBFNN [13], ANFIS [14], and Fuzzy Logic Control (FLC) [15]. However, the need for tracking data and sophisticated fuzzy inference methods is incompatible with lower-cost microcontrollers due to their large neurone count. The performance of genetic algorithms decreases with population growth and does not ensure the best result [16]. However, for precise maximum power point (MPP) exploration, MPPT methods that use soft computing are recommended [17]. The Marine Predictor Algorithm (MPA) exhibits many rounds leading to problems in tracking [18]. Comparing the performance of other MPPT strategies, [19] found that the Ant Colony Optimisation (ACO) method is more efficient, has a very fast tracking, and is comparatively easier to construct than other algorithms described in the literature. In. [20] have applied the Falcon Optimization technique for quick PV power tracking. The behaviour that offers quick global searching and convergence has been studied under partial shade conditions. Transformer-based MPPT systems offer several advantages, primarily including voltage isolation, which enhances system safety and allows flexible voltage level adaptation. However, these systems also have notable disadvantages: they tend to be bulkier, heavier, and more expensive due to the physical transformer component. They may also introduce additional power losses from core and copper losses, which reduce overall system efficiency, especially at light loads [21]. In contrast to other methods reported in the literature, the Ant Lion Optimised ANFIS-based MPPT technique has been used in this paper to obtain acceptable solutions with the highest tracking accuracy.

To meet load requirements, several DC-DC converters have been analysed for MPPT purposes [22]. Typically, buck, boost, buck-boost [23], Zeta [24], Cuk [25], and Single-ended primary-inductor converters (SEPIC) [26]. The buck-boost converter is unable to control MPPT operations as the weather changes. Furthermore, conventional converters need expensive driver circuits with an additional blocked diode to stop battery reversal current [27]. Cuk converters can provide MPPT operation across all PV features under all changing operating situations with minimal input current ripple, although the efficiency of this converter is poor. Modular Multilevel Converters offer significant advantages, such as high scalability, allowing easy adjustment of voltage and power levels by adding or removing submodules. However, MMCs have some disadvantages, including complex control requirements, since balancing the capacitor voltages of each submodule demands sophisticated algorithms. They also involve high component counts, which can increase the initial cost, weight, and size of the converter [28]. Henceforth, in this research work, a Hybrid High-gain Zeta-Cuk converter is employed for improving the power conversion efficiency by minimizing losses. The related analysis based on the converter with MPPT approaches is shown in Table 1.

Table 1: Survey Related to Converter and MPPT Topologies

References	Methodology	Merits	Challenges
[29]	Buck-Boost with P&O	Provide a consistent and highly tracked power supply	High Complexity and high cost
[30]	Fuzzy with boost	Improved Efficiency is achieved	Inaccurate data and depend on human knowledge
[31]	SEPIC with FFA	Higher voltage gain and convergence speed	Complexity in terms of overshoot, tracking efficiency
[32]	Sliding mode control with boost	Enhanced overall proficiency and conversion system	Tuning of this controller is highly challenging.
[33]	GWO-ANFIS with boost	Better stability and a high voltage conversion ratio	It takes more time to converge

Based on the limitations faced by the traditional converters and MPPT techniques, the proposed topology aims to overcome this by providing foremost contributions as given below.

- The integration of renewable PV energy into the operation of BLDC motors for EVs enables clean energy, reducing dependency on fossil fuels and supporting the transition to sustainable transportation.
- The use of a High-Gain Zeta-Cuk converter effectively boosts the low voltage from the PV system to the required voltage levels for the BLDC motor's operation, thereby improving overall system efficiency.
- ALO-ANFIS-based MPPT ensures precise tracking of the extreme power output from the PV system, even under changes in sunlight.
- The Bidirectional DC-DC converter facilitates efficient power distribution between the PV system, battery storage, grid, and BLDC motor.

2. Proposed system modelling

The proposed system comprises multiple interconnected components designed for efficient power management and operation of an EV equipped with a BLDC motor, as exposed in Fig. 1. The PV system output voltage and current are raised by a high-gain Zeta-Cuk converter. This converter enhances the energy transfer efficiency and regulates the DC bus voltage.

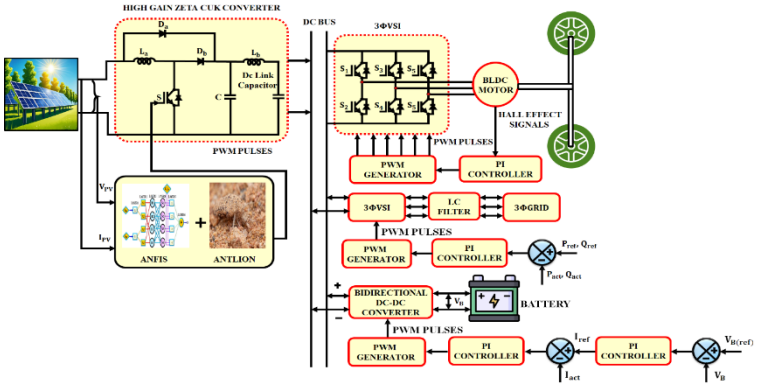

Fig. 1: Block Diagram of PV-Based EV Motor.

An ant lion algorithm-optimized ANFIS-based MPPT receives the output energy from PV for tracking optimal power from PV. Pulse width modulation (PWM) generator drive converter for precise switching and control. The power from the DC bus is directed to the BLDC motor through VSI, speed of the motor is also regulated by the PI controller. For grid interaction, the power is supplied to the VSI, with a PI controller ensuring synchronization and stability by comparing reference and actual power. Additionally, a bidirectional DC-DC converter interfaces the DC bus with a battery storage system, enabling energy storage during surplus generation and power delivery during demand. The battery's voltage and current are controlled by PI controllers to ensure safe operation by comparing reference and actual values. Thereby, the continuous energy is supplied to the BLDC motor for EV.

2.1. Modelling of PV system

A PV module in Fig. 2 is one of the power-producing components and has the potential of providing clean energy to the distribution side. Equation (1) provides Kirchhoff's rule, which determines the current generator from the solar system.

$$I_{PV} = I_L - I_d - I_{sh} \quad (1)$$

Here,I_L specifies the current generator and is defined in the following equation,

$$I_L = G[I_{SC}[1 + k_a](T - T_{STC})] \quad (2)$$

Where, T indicates the ambient temperature of the climate conditions, I_{SC} indicates short short-circuit current of the PV cell, G denotes solar irradiation, T_{STC} shows T of a PV cell under Standard Test Conditions (STC), k_a refer to the temperature coefficient and I_d shows the current of the PV diode that is stated by Shockley's equation below.

$$I_d = I_o\left\{\exp\left(\frac{qV_d}{nKT}\right) - 1\right\} \quad (3)$$

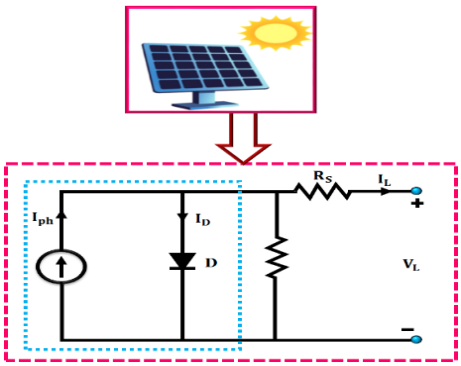

Fig. 2: Overview of PV Module Equivalent Circuit.

The I-V characteristics of a PV cell are derived as follows,

$$I_{PV} = I_L - I_o\left[\exp\left(\frac{q(V_{PV}+IR_S)}{nKT}\right) - 1\right] - \left[\frac{V_{PV}+IR_S}{R_{sh}}\right] \quad (4)$$

I_{PV} and V_{PV}presents PV current and voltage, although the output provided by PV is low owing to the varying temperature and irradiance, so it should be boosted to a higher level to maintain a suitable power to the DC bus; thus, in this study, a high-gain Zeta-Cuk converter is utilized as demonstrated in the section below.

2.2. High-gain zeta-cuk converter

The converter in Fig. 3 is designed to increase the low voltage from PV to a much higher level for the BLDC motor. This converter combines two well-known converters, Zeta and Cuk, to provide high voltage gain while maintaining good efficiency. Fig. 4 represents the switching state. The operating mode of this converter are discussed in the following,

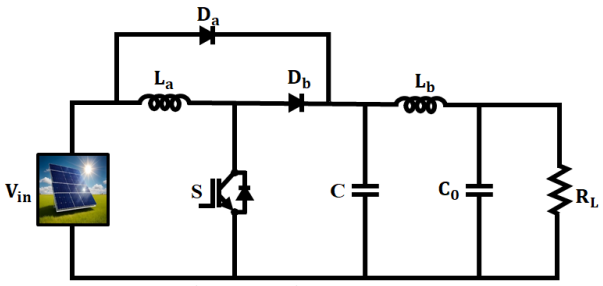

Fig. 3: Circuit Configuration of High Gain Zeta-Cuk Converter.

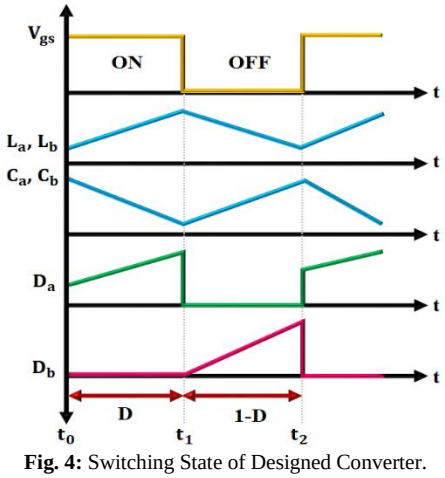

Fig. 4: Switching State of Designed Converter.

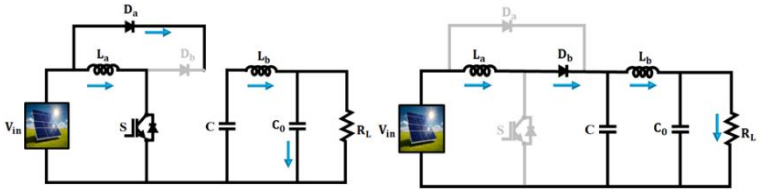

Fig. 5: Modes of Operation for the Proposed Converter.

Mode 1: the switch (S) is in the ON state as in Fig. 5, allowing current to flow through the inductors (L_a andL_b), which enter their charging phase, storing energy from the input source. During this phase, the diode $D_b It\ It$ is in the OFF state, preventing reverse current flow. Simultaneously, the capacitors (C and C_0) discharge, transferring their stored energy to the load.
Mode 2: The switch (S) turns OFF, and the diode D_b becomes ON, allowing the inductors (L_a andL_b) to release their stored energy to the capacitors (C and C_0) and the load. At the same time, the capacitors enter their charging phase, replenishing their energy for the next cycle. These alternating modes of operation ensure efficient energy transfer and voltage regulation.
By applying KVL,

$$V_{PV} = V_{La} \tag{5}$$

$$V_{PV} = V_C \tag{6}$$

From Equations (5) and (6), the following equation is defined as,

$$V_{PV} = V_{La} = V_C \tag{7}$$

$$V_C - V_{Lb} - V_{Co} = 0 \tag{8}$$

$$V_{Co} = V_{RL} = V_0 \tag{9}$$

On substituting (9) in (8),

$$V_C - V_{Lb} - V_0 = 0 \tag{10}$$

$$V_0 = V_C - V_{Lb} \tag{11}$$

Substituting (6) in (5)

$$V_{Lb} = V_{PV} - V_0 \tag{12}$$

By applying KVL in mode 2,

$$V_{PV} - V_{La} - V_C = 0 \tag{13}$$

$$V_C - V_{Lb} - V_0 = 0 \tag{14}$$

$$V_C = V_{Lb} + V_0 \tag{15}$$

On substituting equation (15) in (13)

$$V_{PV} - V_{La} - V_{Lb} = V_0 \tag{16}$$

$$V_{Lb} = V_{PV} - V_{La} - V_0 \tag{17}$$

By substituting (17) in (14)

$$V_C - (V_{PV} - V_{La} - V_0) - V_0 = 0 \tag{18}$$

$$V_C = V_{PV} - V_{La} \tag{19}$$

On applying inductor voltage time balance principle,

$$\int V_{La}\,dt + \int V_{Lb}\,dt = 0 \tag{20}$$

$$V_{La}.D + V_{Lb}(1 - D) = 0 \tag{21}$$

$$V_{Lb} = \frac{D}{1-D} V_{La} \tag{22}$$

On substituting Equation (14) in (16),

$$V_0 = V_{PV} - V_{La} - \left(\frac{D}{1-D}.V_{La}\right) \tag{23}$$

By simplifying Equation (23) as,

$$V_0 = V_{PV}.\frac{D}{1-D} \tag{24}$$

The voltage gain is expressed as,

$$G = \frac{D}{1-D} \tag{25}$$

Overall, by the use of designed converter, higher efficiency is accomplished and the needed power is distribute to the BLDC motor fed EV applications. The Following section details the ALO-ANFIS based MPPT for the goal of tracking available power from PV module.

2.3. Modelling of ANFIS controller

The benefits of ANN and FLC algorithms are combined in the ANFIS-based intelligent MPPT controller, which manage the PV panel's non-linear behavior and offers fast convergence speed and quick dynamic reaction in a range of weather situations. This ANFIS- MPPT controller effectively achieves high tracking accuracy and impedance equivalent functions over PV panel and grid. Training data for the input and output maps has been established by considering the appropriate epochs. For different inputs, inference rule basis system determines an optimal output. In order to set input and output map trained data, enough epochs were considered. When the inputs fluctuate, inference rule base system determines proper output. ANFIS-based MPPT controller structure in Fig. 6 is represented in Fig.6. The assigned membership function is modified by the ANFIS using a series of fuzzy inference rules until the error is minimized and the intended consequence is attained.

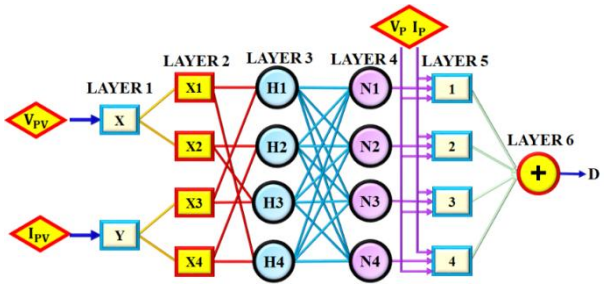

Fig. 6: Configuration of ANFIS Based MPPT Controller.

Also, the progress of membership function is illustrated in Fig.7, the three main control components of the fuzzy logic controller are the defuzzifier, rule basis and fuzzifier. To fuzzify the inputs, the membership functions are assigned.

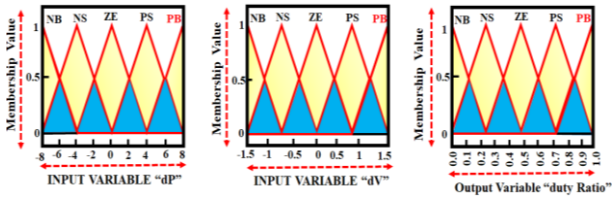

Fig. 7: Overview of Membership Function dP, dV, and Duty Ratio.

Defuzzification using the centroid approach yields the required duty ratio. The weight mean is determined mathematically as follows:

$$W = \frac{\sum_{i=1}^{N} W_i \times \mu(W_i)}{\sum_{i=1}^{N} W_i \times \mu(W_i)} \tag{26}$$

However, the performance of ANFIS heavily depends on the tuning of its parameters. Here, a method based on the Ant Lion Optimization algorithm is utilized for the best ANFIS membership function adjustment as discussed below.

2.4. Antlion optimization

The antlion algorithm in Fig. 8 simulates the interacting between ants inside cones and antlions. The antlion hunts ants in a trap, representing the relationship. The ants browse and the food ant forages stochastically. To imitate the random walks, by the following steps:

$$Z(s) = \left[0, cm\left(2r(s_1 - 1)\right), cm(2r(s_2 - 1), cm(2r(s_3 - 1), \ldots., (2r(s_1 - 1)\right] \tag{27}$$

The symbols cm, n, s, and $r(s)$ represent the cumulative total, the highest number of iterations, the random walk steps, and the stochastic parameter in Equation (9).

$$\begin{cases} 1 \text{ if } rmg > 0 \\ 0 \text{ if } rng \leq 0 \end{cases} \tag{28}$$

Where rng signifies a random number produced using a uniform distribution in the interval [0, 1].

$$M_{ant} = \begin{bmatrix} T_{1,1} & T_{1,2} & \ldots\ldots & T_{1,d} \\ T_{2,1} & T_{2,2} & \ldots\ldots & T_{2,d} \\ \ldots\ldots & \ldots\ldots & \ldots\ldots & \ldots\ldots \\ T_{n,1} & T_{n,1} & \ldots\ldots & T_{n,1} \end{bmatrix} \quad (29)$$

The matrix,M_{antl}, $T_{i,j}$,n, and d stores the value, dimension, total number of ants, and movement dimensions of i-th ant. The objective function is denoted by f. Equation (30) contains matrices for storing ant locations, best fits, and ant lion hunting positions and Fig. 8 depicts the flowchart for the entire process.

$$M_{OA} = \begin{bmatrix} f(T_{1,1} & T_{1,2} & \ldots\ldots & T_{1,d}) \\ fT_{2,1} & T_{2,2} & \ldots\ldots & T_{2,d} \\ \ldots\ldots & \ldots\ldots & \ldots\ldots & \ldots\ldots \\ fT_{n,1} & T_{n,1} & \ldots\ldots & T_{n,1} \end{bmatrix} \quad (30)$$

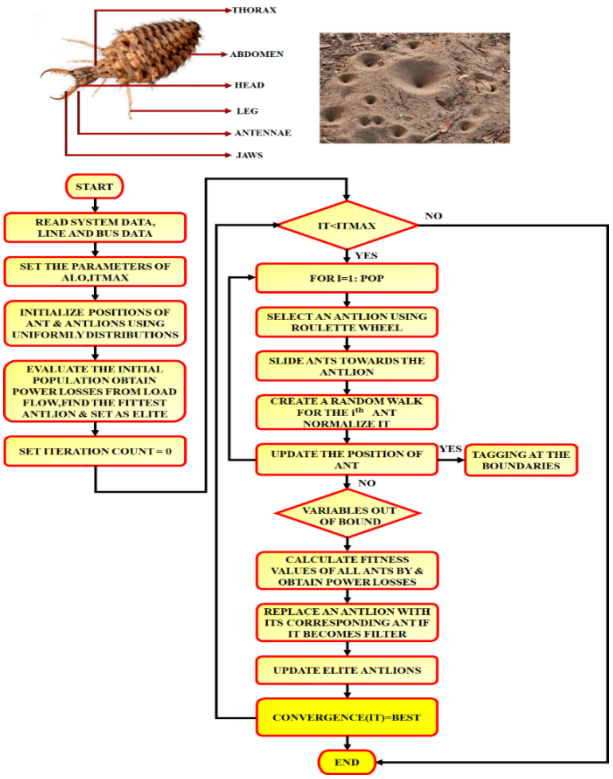

Fig. 8: Flowchart of ALO-ANFIS Based MPPT.

$$M_{antlion} = \begin{bmatrix} N_{1,1} & N_{1,2} & \ldots\ldots & N_{1,d} \\ N_{2,1} & N_{2,2} & \ldots\ldots & N_{2,d} \\ \ldots\ldots & \ldots\ldots & \ldots\ldots & \ldots\ldots \\ N_{n,1} & N_{n,1} & \ldots\ldots & N_{n,1} \end{bmatrix} \quad (31)$$

$$M_{OAL} = \begin{bmatrix} f(N_{1,1} & N_{1,2} & \ldots\ldots & N_{1,d}) \\ f(N_{2,1} & N_{2,2} & \ldots\ldots & N_{2,d}) \\ \ldots\ldots & \ldots\ldots & \ldots\ldots & \ldots\ldots \\ f(N_{n,1} & N_{n,1} & \ldots\ldots & N_{n,1)} \end{bmatrix} \quad (32)$$

M_{OAL} is the matrix used to hold antlion values, $N_{i,j}$denotesdimension of i-th antlion, n is number of antlions, and f is the objective function. To optimize the objective function with the ALO, make the following assumptions. Ants maximize their chances of finding food by moving randomly in all directions. Equations (31) and (32) show how ants move randomly in a search space while avoiding pits, affecting their random movement. The first antlion to catch an ant is considered the fittest, as each antlion can catch all other ants. The ants' random migration near antlions gradually reduces over time.

Table 2: Parameters of ALO-ANFIS

Parameters	Values
Number of training epochs	100
Number of membership functions	3 per input variable
Type of membership function	Gaussian
Input variables	Change in power, change in voltage
Output variable	Duty cycle
Population size	50
Maximum iterations	100
Search space boundaries	[0,1]
Rule base structure	9 rules (for 3 MFs/input)

Table 2 denotes the parameters of ALO-ANFIS. With the help of MPPT topologies, the highest amount of energy from the PV module is highly tracked with higher efficiency. Subsequently, the energy is transferred to the BLDC motor over a phase VSI.

2.5. Modelling of BLDC motor

BLDC motors are appropriate for electric vehicle applications because of their high efficiency, small size, and superior torque characteristics. The following equation is used to express the mathematical model when applying Kirchhoff's defined voltage law to the three-phase stator loop winding circuits shown in equations (33-35), and (36).

$$V_p = R_p i_p + L_p \frac{di_p}{dt} + M_{pq} \frac{di_r}{dt} + e_p \tag{33}$$

$$V_q = R_q i_q + L_q \frac{di_q}{dt} + M_{qr} \frac{di_r}{dt} + e_q \tag{34}$$

$$V_r = R_r i_r + L_r \frac{di_r}{dt} + M_{rp} \frac{di_q}{dt} + e_r \tag{35}$$

V_p, V_q, and V_r stands for the BLDC motor's voltage across a phase, R_p, R_q, R_rIndicate the stator winding resistance, and i_p, i_q, i_rCalculate the phase current of $P, Q,$ and R windings of the BLDC motor as in Fig. 9. M_{pq}, M_{qr}, M_{rp}How is the stator winding mutual inductance as indicated in equation (37) below,

$$\begin{bmatrix} L_p & M_{pq} & M_{pr} \\ M_{qp} & L_q & M_{qr} \\ M_{rp} & M_{rq} & L_r \end{bmatrix} \frac{di}{dt} \begin{bmatrix} L_p \\ L_q \\ L_r \end{bmatrix} = \begin{bmatrix} V_p \\ V_q \\ V_r \end{bmatrix} - \begin{bmatrix} R_p & 0 & 0 \\ 0 & R_q & 0 \\ 0 & 0 & R_r \end{bmatrix} - \begin{bmatrix} e_p \\ e_q \\ e_r \end{bmatrix} \tag{36}$$

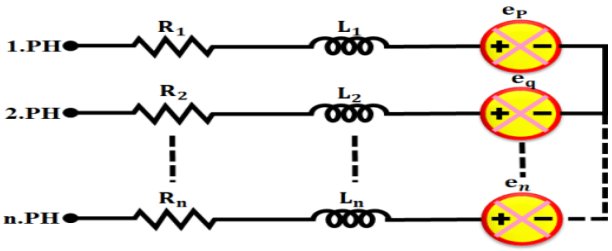

Fig. 9: Circuit of BLDC Motor.

The electromagnetic torque produced by this three-phase BLDC motor is influenced by the speed, back-EMF, and current waveforms that are applied. Thus, the instantaneous electromagnetic torque is expressed by equation (37), which is

$$T_{em} = J \frac{d\omega_r}{dt} + B\omega + T_L \tag{37}$$

Whereω, B, J stands for a distinct element of the motor's moment of inertia, frictional coefficient, and angular velocity, respectively. The torque under load is indicated by T_LConsequently, the instantaneous electromagnetic torque is expressed by equation (38).

$$T_{em} = \frac{1}{\omega_m}\left(e_p i_p + e_q i_q + e_r i_r\right) \tag{38}$$

The BLDC motor speed is effectively managed by a PI controller for improving the performance for EV applications. Despite this, excess energy from PV is provided to the grid through a VSI and battery system. Moreover, the bidirectional battery converter performs an essential role in charging and discharging based on the battery requirement, as discussed below.

2.6. Modelling of bidirectional converter

A bidirectional converter is designed to function in both discharging (Boost mode) and charging (Buck mode) scenarios, as in Fig. 10. An API controller is incorporated, which effectively manages both modes, simplifying the control system and ensuring seamless operation and transitions.

In boost mode, S_2 facilitates the transfer of energy from the input side to the output side. When S_2When turned on, the capacitor releases energy to the output terminal, and the inductor stores energy. When S_2 is turned off, the inductor charges the capacitor C through the current flowing via the diode D_1. This charging process ensures the proper functioning of the converter in boost mode.

In buck mode, S_1 transfers energy from the output terminal to the input terminal. When S_1 is activated, current flows to the input, and during S_2 is turned off, the stored energy in the inductor is released and flows through the diode D_2, maintaining the current flow until $S_1 It$ is turned on again. This continuous energy transfer ensures the proper functioning of the converter in buck mode. Overall, the EV motor gets an adequate power supply with the assistance of the proposed topology, with better performance analysis.

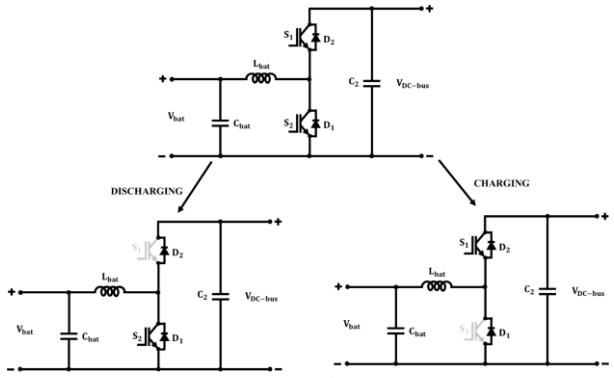

Fig. 10: Operational Modes of Bidirectional Converter.

3. Results and discussion

This section focuses on outcomes of a developed high-gain Zeta-Cuk converter with ALO-ANFIS-based MPPT working with a BLDC motor from the MATLAB/Simulink analysis with parameters indicated in Table 3. Different conditions like varying and constant temperature and intensity, as well as varying motor speed and applying load conditions, are detailed below for validating the proposed system. Additionally, comparative performance is made over classical topologies, which illustrates the advantage of the proposed converter and MPPT strategies. Table 2 describes the parameter specification for PV PV-based converter for the BLDC motor.

Table 3: Parameter Evaluation for the Proposed System

Parameter	Description
Solar PV System	
Short circuit Current	8.95A
Series Connected solar PV cell	4
Parallel Connected solar PV cell	6
Maximum power Voltage	29.95V
Maximum Current	8.35A
High gain Zeta-Cuk converter	
Switching Frequency	10kHz
C	22µF
C_o	2200 µF
L_a, L_b	1.1mH

a) Case 1- Variation in temperature and intensity

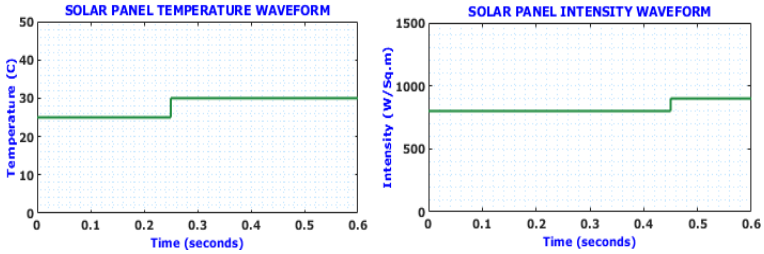

Fig. 11: Temperature and Intensity Waveforms for Case 1 Condition.

The temperature of the solar panel and solar irradiance vary dynamically over time, as shown in Fig. 11. Initially, the temperature rises and reaches a steady value of 30°C, while the intensity fluctuates, demonstrating an unsteady environment, and after 0.45s, it is continuously maintained at 900(W/Sq. m). The voltage output of the solar panel adjusts in response to the varying conditions, showing slight oscillations before stabilizing at 330V. The input current decreases significantly in the first 0.1 seconds and then stabilizes at 30A as the system adapts to changing conditions. The output voltage drops initially and indicates efficient voltage regulation by the converter by providing a stable voltage at -600 after a duration of 0.45s, as represented in Fig. 12. The output current also stabilizes after an initial transient dip, reflecting the converter's effective current regulation by maintaining a steady output at -16A. Specifically, the output voltage waveform shows a sharp peak, reaching a high negative value before stabilizing to its intended steady-state level. Similarly, the output current exhibits an initial surge, dropping to a negative peak before gradually settling. These overshoots are typical during the startup phase as the converter components, particularly the inductors and capacitors, respond to sudden energy transfer and system stabilization. The input power exhibits fluctuations before settling, while the output power rises steadily and stabilizes as shown in Fig. 13, demonstrating the system's ability to handle variations and maintain consistent output.

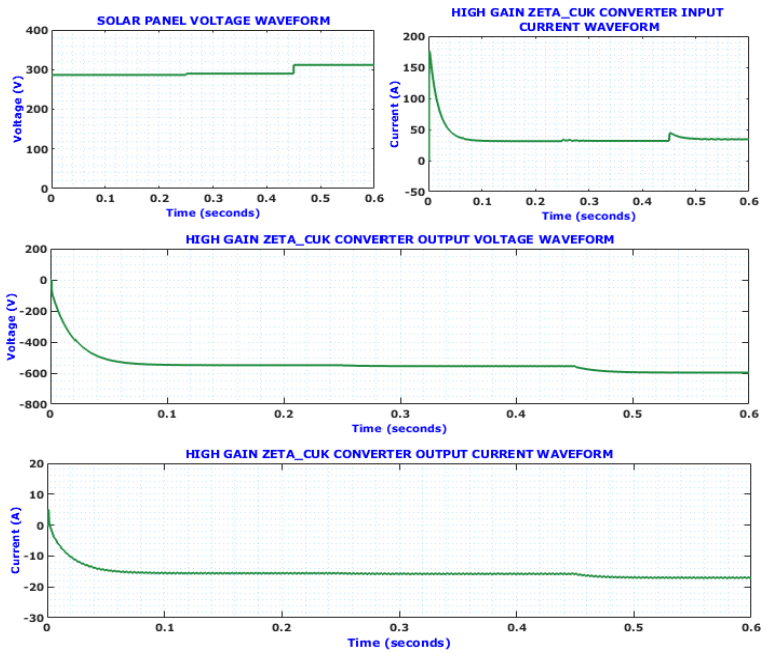

Fig. 12: Solar Module and Converter Waveforms for Case 1 Condition.

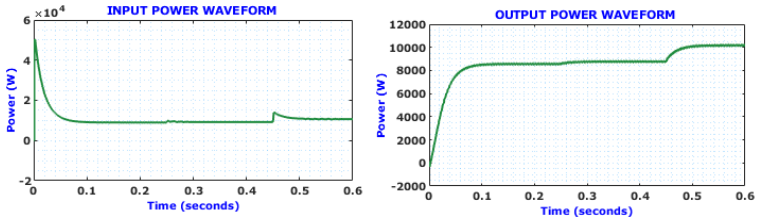

Fig. 13: Input and Output Power Waveforms.

b) Case 2: Constant Temperature and Intensity

In a constant solar panel temperature and intensity waveform, both temperature and intensity remain constant at $30°C$ and $900(W/Sq.m)$ throughout the period as denoted in Fig. 14, simulating stable environmental conditions. The voltage output of the solar panel remains steady at 330V without significant variations due to the constant operating conditions. The input current initially decreases rapidly and then remains steady, reflecting minimal fluctuations under constant conditions. High-Gain Zeta-Cuk Converter output voltage exhibits a rapid initial drop before stabilizing at 600V as specified in Fig. 15, indicating the converter's ability to maintain a steady output under fixed conditions with the aid of ALO-ANFIS-based MPPT. Likewise, the output current also shows transient fluctuations before stabilizing --16A. Both input and output power waveforms are steady after an initial transient phase, as indicated in Fig. 16, highlighting the system's efficiency under constant environmental conditions.

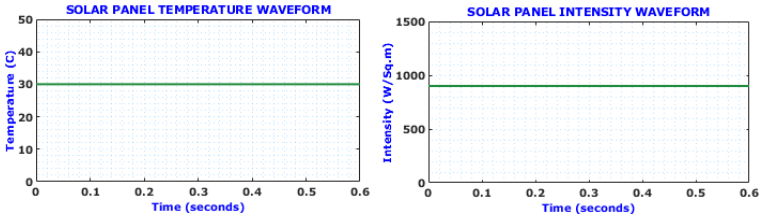

Fig. 14: Temperature And Intensity Waveforms for Case 2 Condition.

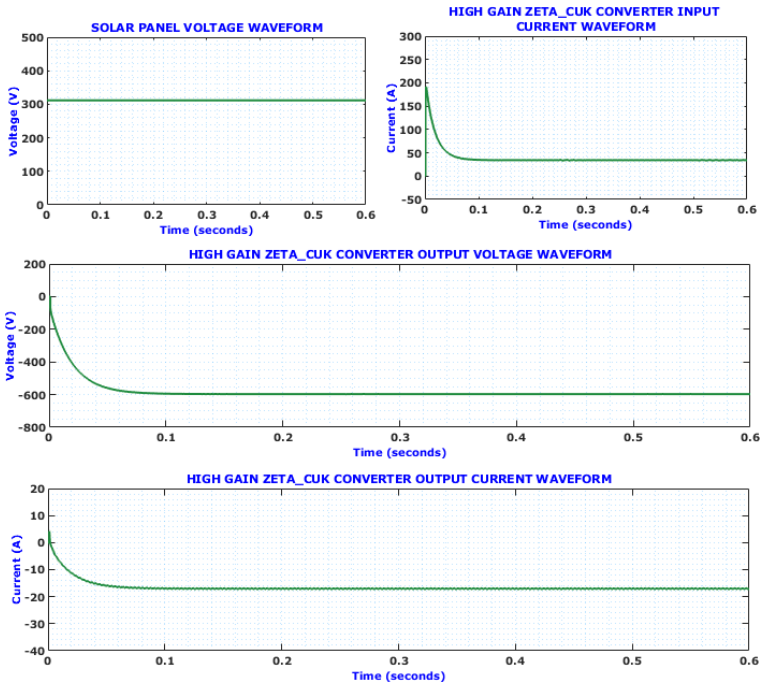

Fig. 15: Solar Module and Converter Waveforms for Case 2 Condition.

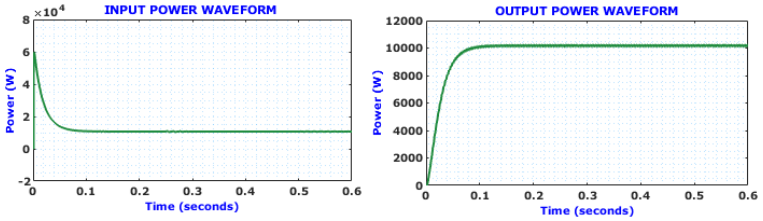

Fig. 16: Input and Output Power Waveforms.

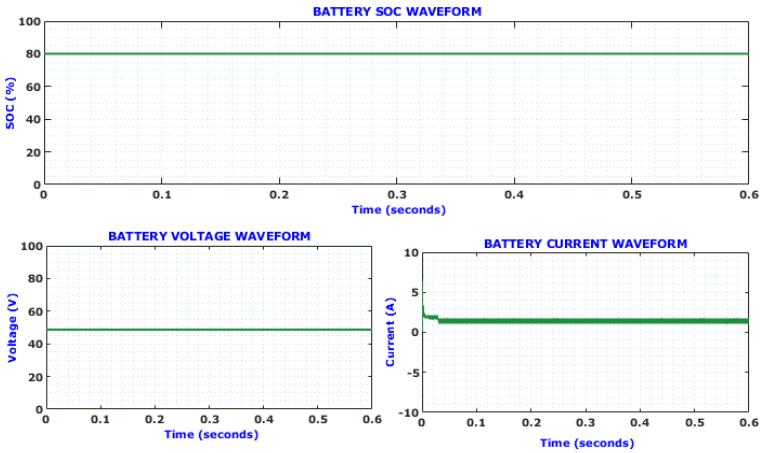

Fig. 17: Battery Waveforms.

The SOC remains constant at approximately 80% throughout 0.6 seconds, indicating a fully charged battery that is neither charging nor discharging significantly. The battery voltage is steady at around 50V throughout the time, as illustrated in Fig. 17, reflecting stable operating conditions without significant load or input changes. The battery current shows minimal power flow to or from the battery after the initial transient and remains at 1.5A. The grid voltage is sinusoidal and oscillates consistently between ±430 V, indicating a stable AC supply. The grid current also oscillates sinusoidally between ±12A, maintaining synchronization with the voltage waveform shown in Fig. 18. The real power remains constant, indicating steady energy transfer under load. The reactive power shows consistent reactive energy management as described in Fig. 19, typical in systems with inductive or capacitive components.

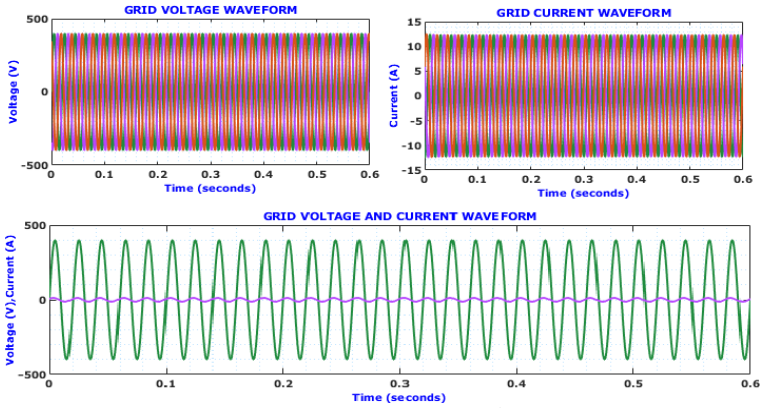

Fig. 18: Three Phase Grid Waveforms.

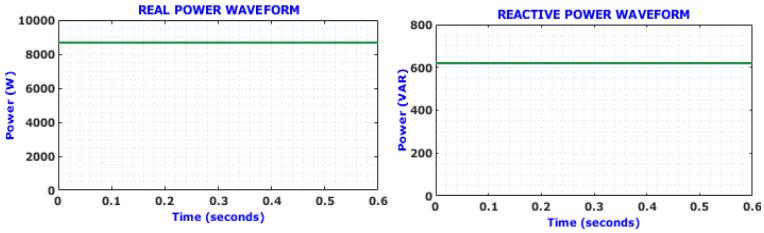

Fig. 19: Real and Reactive Power Waveforms.

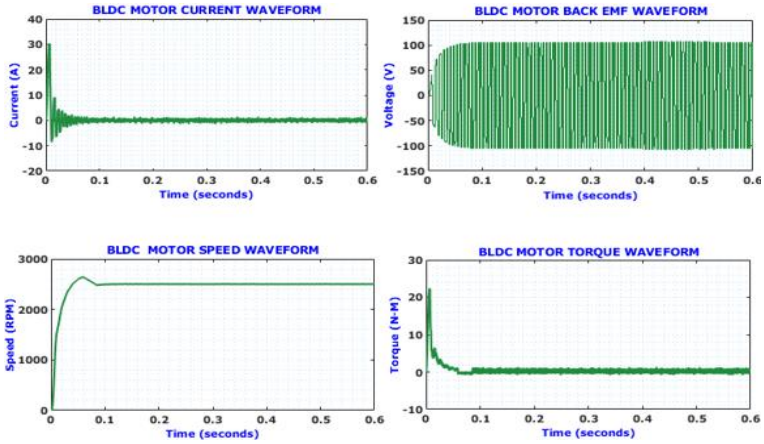

Fig. 20: BLDC Motor Waveforms.

The BLDC motor current starts with a peak of around 30A, then decreases and stabilizes near 10A after 0.1s. The back EMF sinusoidally maintains between ±100 V after 0.1s, representing the normal electromagnetic behavior of the motor at constant speed as shown in Fig. 19. The motor speed rapidly increases and maintains at 2500 RPM after 0.1s, showing efficient speed regulation. The torque starts at around 20 Nm, then decreases and stabilizes near 10 Nm after 0.1 seconds, corresponding to steady-state operation under constant load.

c) BLDC test Case 1- under varying speed from 2000-2500 RPM

The BLDC motor initially operates at 2000 RPM and maintains this speed until approximately 0.35 seconds. Afterward, the speed increases to 2500 RPM and stabilizes, demonstrating the motor's ability to handle speed transitions smoothly. The motor torque starts near 5Nm and remains steady throughout the duration as specified in Fig. 21. There are no significant variations in torque, indicating stable operation under varying speed conditions.

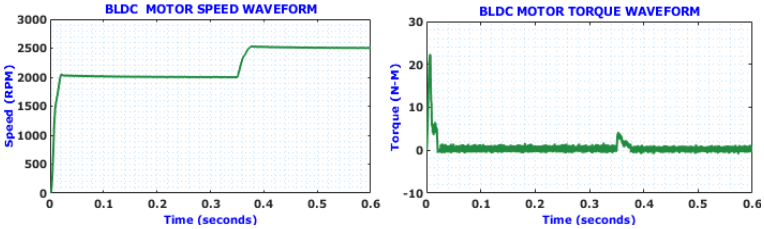

Fig. 21: BLDC Motor Under Varying Speed from 2000-2500 RPM.

d) BLDC test Case 1- under 2500RPM and apply 1NM load at 0.35s

The motor operates at a constant speed of 2500 RPM throughout the period, even after the application of a load at 0.35 seconds. This highlights the motor's ability to maintain a steady speed under load changes. Initially, the torque is near 0 Nm. At 0.35 seconds, a 1 Nm load is applied, causing a minor transient response as shown in Fig. 22. The torque quickly stabilizes at 1 Nm, demonstrating the system's ability to adapt to load variations efficiently.

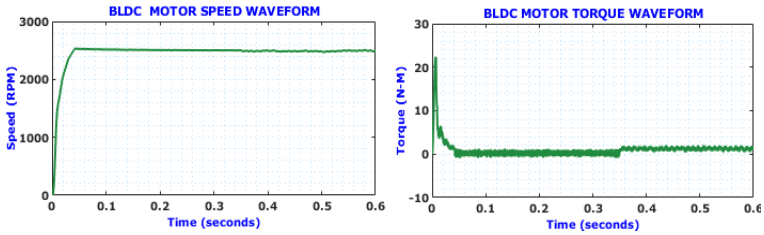

Fig. 22: BLDC Motor Under 2500RPM and Apply 1NM Load at 0.35s.

e) BLDC test Case 1- under 2500RPM and apply 1.5 NM load at 0.35s

The motor operates steadily at 2500 RPM throughout the test period, unaffected by the application of a 1.5 Nm load at 0.35 seconds. This showcases the motor's ability to maintain consistent speed even with higher load demands. At 0.35 seconds, a 1.5 Nm load is applied, causing a slight transient response before stabilizing at 1.5 Nm as illustrated in Fig. 22. The system effectively handles the higher load with minimal disruption.

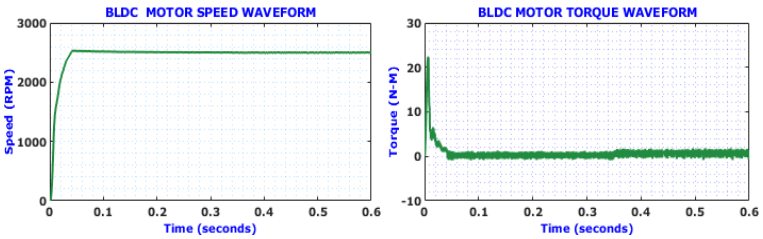

Fig. 23: BLDC Motor Under 2500RPM and Apply 1.5 NM Load at 0.35s.

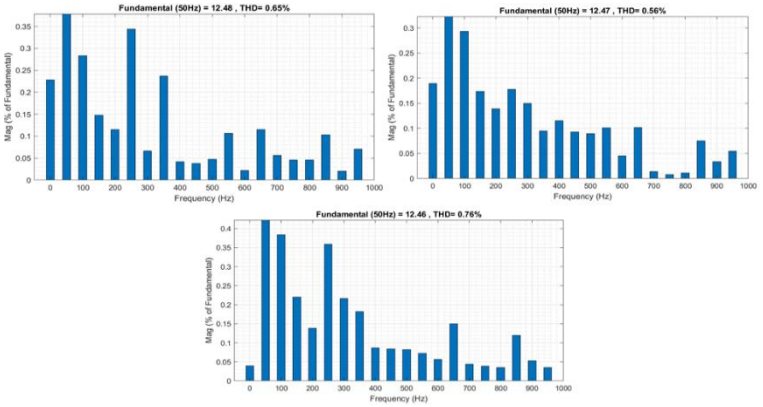

Fig. 24: THD Waveforms (R, Y and B Phases).

With the aid of proposed high gain converter attains lower harmonics value of (0.65%, 0.56% and 0.78%) for R, Y and B phases as represented in Fig. 24, which ensures pure sinusoidal output with high power quality. Table 4 denotes the comparison of converter components.

Table 4: Comparison of Converter Components

Converters	Components Switches	Diodes	Voltage gain Expression
In [39]	2	4	$\frac{3+D}{1-D}$
In [40]	2	4	$\frac{1+D+2n}{1-D}$
In [41]	4	2	$\frac{2+2n}{1-D}$
In [42]	2	6	$\frac{2+2n}{1-D}$
In [43]	1	2	$\frac{2D}{1-D}$
In [44]	2	2	$\frac{D(3+D)}{1-D}$
Proposed	1	2	$\frac{D}{1-D}$

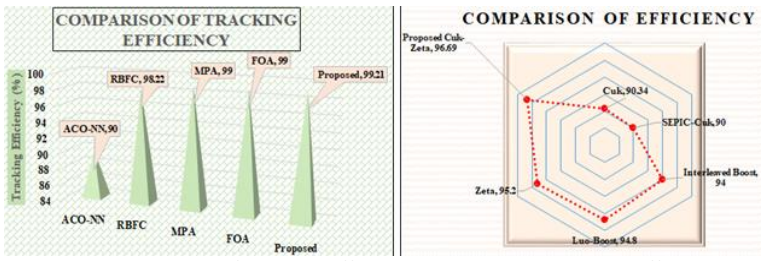

Fig. 25: Comparison of Tracking Efficiency and Voltage Conversion Efficiency.

Fig. 25 shows a bar comparison of voltage conversion efficiency and tracking efficiency among different methods. Efficiency comparison among systems like Cuk, Zeta, Luo-Boost, SEPIC-Cuk, Interleaved Boost, proposed Zeta-Cuk system [34-38] demonstrates the highest efficiency at 96.59%, is accomplished by the proposed high-gain Zeta-Cuk converter, highlighting its superior performance. Similarly, ALO-ANFIS-based MPPT achieves the highest efficiency at 99.21%, outperforming all other methods referred to in [17, 12, 16, 41, 42], respectively. Table 5 represents the comparison of convergence time.

Table 5: Comparison of Convergence Time

MPPT Approaches	Convergence time
MPA [16]	0.1532
RBFC [12]	0.250
AFO [17]	0.88
ACO-ANN [45]	0.16
GWO-ANFIS [46]	0.141
Proposed ALO	0.12

The practical implementation of this advanced EV charging system faces several challenges. Managing the dynamic and intermittent nature of solar energy requires highly responsive and adaptive control, making real-time tuning of the ALO-ANFIS MPPT system computationally intensive. The complexity of coordinating power flow between the PV array, storage battery, grid, and BLDC motor demands robust and reliable bidirectional converter control, which can be sensitive to parameter variations and environmental disturbances. Cost factors, including high-quality components for converters, controllers, and thermal management systems, also pose significant barriers to large-scale deployment.

The proposed high-efficiency EV charging system, integrating a renewable energy source with a high-gain Zeta-Cuk converter and advanced MPPT control, offers a cost-effective solution despite its initial investment. The major costs arise from high-efficiency photovoltaic panels, the high-gain Zeta-Cuk converter components, the bidirectional DC-DC converter setup, and the implementation of intelligent control algorithms using microcontrollers. However, the system's ability to achieve high energy conversion and tracking efficiencies ensures reduced energy losses, lower operating costs, and minimal reliance on grid electricity.

4. Conclusion

This work presents a comprehensive solution for the efficient and sustainable charging of EVs powered by a BLDC motor. The proposed high-efficiency charging system integrates a Renewable Energy-based High-Gain Zeta-Cuk converter, which effectively boosts the low voltage from PV sources to an advanced level appropriate for charging EVs. By employing an ANFIS-ALO algorithm, precise tracking of maximum power despite fluctuating environmental conditions is attained with better tracking efficiency. Additionally, the incorporation of a storage battery and grid system allows for the storage of excess energy generated by PV source. The power distribution between the grid, battery, and BLDC motor is managed efficiently through a Bidirectional DC-DC converter. The simulation results in MATLAB/Simulink demonstrate that the proposed topology achieves superior conversion efficiency of 96.69%) and tracking efficiency of (99.21%) with minimal convergence time, highlighting a sustainable solution for EV charging systems. By enhancing the performance and reliability of solar-powered EV charging, the system directly supports governmental initiatives promoting renewable energy adoption and electric vehicle incentives. The future works can focus on the issues related to computational complexity and integration with smart grids, improving the versatility of the proposed concept.

References

[1] Lakshminarayana G, Rao JV, Avvari RK, "A Review on Electric Vehicle Developments and Battery Management Improvements," *In Congress on Control, Robotics, and Mechatronics*, (2024), pp. 231-242. Singapore: Springer Nature Singapore. https://doi.org/10.1007/978-981-97-7094-6_18.

[2] Abd Aziz MA, Saidon MS, Romli MI, Othman SM, Mustafa WA, Manan MR, Aihsan MZ, "A review on BLDC motor application in electric vehicle (EV) using battery, supercapacitor and hybrid energy storage system: efficiency and future prospects," *Journal of Advanced Research in Applied Sciences and Engineering Technology*, (2023), Vol. 30, No. 2, pp. 41-59. https://doi.org/10.37934/araset.30.2.4159.

[3] Kar BN, Samuel P, Mallick A, Pradhan JK, "Grid-connected solar PV fed BLDC motor drive for water pumping system," *Distributed Generation & Alternative Energy Journal* (2023), pp. 1477-1504. https://doi.org/10.13052/dgaej2156-3306.3856.

[4] Kavin KS, Subha Karuvelam P, Devesh Raj M, Sivasubramanian M, "A Novel KSK Converter with Machine Learning MPPT for PV Applications," *Electric Power Components and Systems* (2024), pp. 1-19. https://doi.org/10.1080/15325008.2024.2346806

[5] Gogoi D, Bharatee A, Ray PK, "Implementation of battery storage system in a solar PV-based EV charging station," *Electric Power Systems Research*, (2024), Vol. 229, pp. 110113. https://doi.org/10.1016/j.epsr.2024.110113.

[6] Kavin KS, Karuvelam PS, Matcha M, Vendoti S, "Improved BRBFNN-based MPPT algorithm for coupled inductor KSK converter for sustainable PV system applications," *Electrical Engineering* (2025), pp. 1-23. https://doi.org/10.1007/s00202-025-02952-9.

[7] Alshareef MJ, "An effective falcon optimization algorithm based MPPT under partial shaded photovoltaic systems," *IEEE Access*, Vol. 10, (2022), pp. 131345-131360. https://doi.org/10.1109/ACCESS.2022.3226654.

[8] Endiz MS, "Design and implementation of microcontroller-based solar charge controller using modified incremental conductance MPPT algorithm," *Journal of Radiation Research and Applied Sciences*, Vol. 17, No. 2, (2024), pp. 100938. https://doi.org/10.1016/j.jrras.2024.100938

[9] Elzein IM, Kurdi M, Harrye Y, "Optimizing the Maximum Power of Photovoltaic System Using Modified Incremental Conductance Algorithm Operating Under Varying Dynamic Climatic Conditions," *Int. J. Comput. Digit. Syst*, Vol. 15, (2024), pp. 1-21. https://doi.org/10.12785/ijcds/150136.

[10] Ait Ayad I, Elwarraki E, Baghdadi M, "Intelligent Perturb and Observe Based MPPT Approach Using Multilevel DC-DC Converter to Improve PV Production System," *Journal of Electrical and Computer Engineering*, Vol. 2021, No. 1, (2021), pp. 6673022. https://doi.org/10.1155/2021/6673022.

[11] Wongsathan R, "Integrated neural network-based MPPT and ant colony optimization-tuned PI bidirectional charger-controller for PV-powered motor-pump system," *Engineering and Applied Science Research*, Vol. 51, No. 5, (2024), pp. 605-617.

[12] Kiran SR, Basha CH, Singh VP, Dhanamjayulu C, Prusty BR, Khan B, "Reduced simulative performance analysis of variable step size ANN based MPPT techniques for partially shaded solar PV systems," *IEEE access*, Vol. 10, (2022), pp. 48875-48889. https://doi.org/10.1109/ACCESS.2022.3172322

[13] Rao CV, Raj RD, Anil Naik K, "A novel hybrid image processing-based reconfiguration with RBF neural network MPPT approach for improving global maximum power and effective tracking of PV system," *International Journal of Circuit Theory and Applications*, (2023), Vol. 51, No. 9, pp. 4397-4426. https://doi.org/10.1002/cta.3629.

[14] Turkay Y, Yüksek AG, "Investigating the Potential of An ANFIS Based Maximum Power Point Tracking Controller for Solar Photovoltaic Systems," *IEEE Access* (2025). https://doi.org/10.1109/ACCESS.2025.3547954

[15] Khan M, Raza MA, Jumani TA, Mirsaeidi S, Ali A, Abbas G, Touti E, Alshahir A, "Modeling of intelligent controllers for solar photovoltaic system under varying irradiation conditions," *Frontiers in Energy Research*, Vol. 11, (2023), pp.1288486. https://doi.org/10.3389/fenrg.2023.1288486

[16] Yao G, Luo Z, Lu Z, Wang M, Shang J, Guerrerob JM, "Unlocking the potential of wave energy conversion: A comprehensive evaluation of advanced maximum power point tracking techniques and hybrid strategies for sustainable energy harvesting," *Renewable and Sustainable Energy Reviews*, Vol. 185, (2023), pp. 113599. https://doi.org/10.1016/j.rser.2023.113599.

[17] Naoussi SR, Saatong KT, Molu RJ, Mbasso WF, Bajaj M, Louzazni M, Berhanu M, Kamel S, "Enhancing MPPT performance for partially shaded photovoltaic arrays through backstepping control with Genetic Algorithm-optimized gains," *Scientific Reports*, Vol. 14, No. 1, (2024), pp. 3334. https://doi.org/10.1038/s41598-024-53721-w.

[18] Radhakrishnan RK, Marimuthu U, Balachandran PK, Shukry AM, Senjyu T, "An intensified marine predator algorithm (MPA) for designing a solar-powered BLDC motor used in EV systems," *Sustainability*, Vol. 14, No. 21, (2022), pp. 14120. https://doi.org/10.3390/su142114120.

[19] Xia K, Li Y, Zhu B, "Improved photovoltaic MPPT algorithm based on ant colony optimization and fuzzy logic under conditions of partial shading," *IEEE Access* (2024). https://doi.org/10.1109/ACCESS.2024.3381345.

[20] Bollipo RB, Mikkili S, Bonthagorla PK, "Hybrid, optimal, intelligent and classical PV MPPT techniques: A review," *CSEE Journal of Power and Energy Systems*, Vol. 7, No. 1 (2020), pp. 9-33. https://doi.org/10.17775/CSEEJPES.2019.02720.

[21] Agrawal P, Bansal HO, Gautam AR, Mahela OP, Khan B, "Transformer-based time series prediction of the maximum power point for solar photovoltaic cells," *Energy Science & Engineering* (2022), Vol. 10, No. 9, pp. 3397-3410. https://doi.org/10.1002/ese3.1226

[22] Revathi BS, Prabhakar M, "Solar PV fed DC microgrid: Applications, converter selection, design and testing," *IEEE access*, Vol. 10, (2022), pp. 87227-87240. https://doi.org/10.1109/ACCESS.2022.3199701.

[23] Meshael H, Elkhateb A, Best R, "Topologies and design characteristics of isolated high step-up DC–DC converters for photovoltaic systems," *Electronics*, Vol. 12, No. 18, (2023), pp. 3913. https://doi.org/10.3390/electronics12183913

[24] Valdez-Resendiz JE, Mayo-Maldonado JC, Alejo-Reyes A, Rosas-Caro JC, "Double-dual dc-dc conversion: A survey of contributions, generalization, and systematic generation of new topologies," *IEEE Access*, Vol: 11, (2023), pp. 38913-38928. https://doi.org/10.1109/ACCESS.2023.3268230

[25] Shukla T, Nikolovski S, "A Bridgeless Cuk-BB-Converter-Based BLDCM Drive for MEV Applications," *Energiesn*, Vol. 16, No. 9, (2023), pp. 3747. https://doi.org/10.3390/en16093747

[26] Madrid E, Murillo-Yarce D, Restrepo C, Muñoz J, Giral R, "Modelling of SEPIC, ćuk and zeta converters in discontinuous conduction mode and performance evaluation," *Sensors*, Vol. 21, No. 22, (2021), pp. 7434. https://doi.org/10.3390/s21227434.

[27] Djilali AB, Yahdou A, Benbouhenni H, Alhejji A, Zellouma D, Bounadja E, "Enhanced perturb and observe control for addressing power loss under rapid load changes using a buck–boost converter," *Energy Reports*, Vol.12, (2024), pp. 1503-1516. https://doi.org/10.1016/j.egyr.2024.07.032

[28] Bashir SB, Ismail AA, Elnady A, Farag MM, Hamid AK, Bansal RC, Abo-Khalil AG, "Modular multilevel converter-based microgrid: a critical review," *IEEE Access*, (2023), Vol. 11, pp. 65569-65589. https://doi.org/10.1109/ACCESS.2023.3289829

[29] Maaruf M, Khan K, Khalid M, "Robust control for optimized islanded and grid-connected operation of solar/wind/battery hybrid energy," *Sustainability*, Vol. 14, No. 9, (2022), pp. 5673, https://doi.org/10.3390/su14095673.

[30] Muralikumar K, Ponnambalam P, "Comparison of Fuzzy and ANFIS Controllers for Asymmetrical 31-Level Cascaded Inverter with Super Imposed Carrier PWM Technique," *IEEE Access*, Vol. 2021, No. 9, pp. 82630–82646. https://doi.org/10.1109/ACCESS.2021.3086674.

[31] Priyadarshi N, Bhaskar MS, Sanjeevikumar P, Azam F, Khan, "High-power DC–DC converter with proposed HSFNA MPPT for photovoltaic based ultra-fast charging system of electric vehicles," *IET Renew.Power Gener*., Vol. 16, No. 9, (2022). https://doi.org/10.1049/rpg2.12513

[32] Hamed SB, Abid A, Hamed MB, Sbita L, Bajaj M, Ghoneim SS, Zawbaa HM, Kamel S, "A robust MPPT approach based on first order sliding mode for triple-junction photovoltaic power system supplying electric vehicle," *Energy Rep.*, Vol. 9, (2023), pp. 4275–4297. https://doi.org/10.1016/j.egyr.2023.02.086

[33] Mazumdar D, Biswas PK, Sain C, Ahmad F, Al-Fagih L, "A robust MPPT framework based on GWO-ANFIS controller for grid-tied EV charging stations," *Scientific Reports*, Vol. 14, No. 1 (2024), pp. 30955. https://doi.org/10.1038/s41598-024-81937-3

[34] Pop-Calimanu IM, Balint M, Lascu D, "A new hybrid Ćuk DC-DC converter with coupled inductors," *Electronics*, Vol. 9, No. 12, (2020), pp. 2188. https://doi.org/10.3390/electronics9122188.

[35] Duraisamy M, "Closed-loop Implementation of a Non-isolated High Step-up Integrated SEPIC-CUK DC-DC Converter Structure with Single Switch," *Brazilian Archives of Biology and Technology*, Vol. 67, (2024), pp. e24230787. https://doi.org/10.1590/1678-4324-2024230787

[36] Preethiraj PM, Edward JB, "Design of novel DC-DC interleaved boost converter for BLDC application," *Heliyon*, Vol. 10, No. 22, (2024). https://doi.org/10.1016/j.heliyon.2024.e40041

[37] Gopalasami R, Chokkalingam B, Muthusamy S, "A novel method for hybridization of super lift luo converter and boost converter for electric vehicle charging applications," *Energy Sources, Part A: Recovery, Utilization, and Environmental Effects*, Vol. 45, No. 3, (2023), pp. 8419-8437. https://doi.org/10.1080/15567036.2023.2226104.

[38] Santosh Kumar Reddy PL, Obulesu YP, Singirikonda S, Al Harthi M, Alzaidi MS, Ghoneim SS, "A non-isolated hybrid Zeta converter with a high voltage gain and reduced size of components," *Electronics*, Vol. 11, No. 3, (2022), pp. 483. https://doi.org/10.3390/electronics11030483.

[39] Cui C, Tang Y, Guo Y, Sun H, Jiang L, "High step-up switched-capacitor active switched-inductor converter with self-voltage balancing and low stress," *IEEE Trans. Ind. Electron*., Vol. 69, No. 10, (2022), pp. 10112–10128. https://doi.org/10.1109/TIE.2021.3135611

[40] Guepfrih MF, Waltrich G, Lazzarin TB, "High step-up DC–DC converter using built-in transformer voltage multiplier cell and dual boost concepts," *IEEE J. Emerg. Sel. Topics Power Electron*, Vol. 9, No. 6, (2021), pp. 6700–6712. https://doi.org/10.1109/JESTPE.2021.3063060

[41] Ghaffarpour Sadighi H, Afjei SE, Salemnia A, "High step-up DC–DC converter based on coupled-inductor for renewable energy systems," *IET Power Electron*., Vol. 13, No. 18, (2020), pp. 4315–4324. https://doi.org/10.1049/iet-pel.2020.0310.

[42] Hu X, Liang W, Liu X, Yu Z, "A hybrid interleaved DC–DC converter with a wide step-up regulation range and ultralow voltage stress," *IEEE Trans. Ind. Electron*., Vol. 67, No. 7, (2020), pp. 5479–5489. https://doi.org/10.1109/TIE.2019.2931264.

[43] Duraisamy M, "Closed-loop Implementation of a Non-isolated High Step-up Integrated SEPIC-CUK DC-DC Converter Structure with Single Switch," *Brazilian Archives of Biology and Technology*, (2024), Vol. 67, pp. e24230787. https://doi.org/10.1590/1678-4324-2024230787.

[44] Li H, Cheng L, Sun X, Li C, "High step-up combined boost-Cuk converter with switched-inductor," *IET Power Electronics*, (2022), Vol. 15, No. 15, pp. 1664-1674. https://doi.org/10.1049/pel2.12335.

[45] Babes B, Boutaghane A, Hamouda N, "A novel nature-inspired maximum power point tracking (MPPT) controller based on ACO-ANN algorithm for photovoltaic (PV) system fed arc welding machines," *Neural Computing and Applications*, (2022), Vol. 34, No. 1, pp. 299-317. https://doi.org/10.1007/s00521-021-06393-w

[46] Mazumdar D, Biswas PK, Sain C, Ahmad F, Al-Fagih L, "A robust MPPT framework based on GWO-ANFIS controller for grid-tied EV charging stations," *Scientific Reports*, (2024), Vol. 14, No. 1, pp. 30955. https://doi.org/10.1038/s41598-024-81937-3.